Model Predictive Torque Control for Torque Ripple Compensation in Variable-Speed PMSMs

Andrés Mora, *Student Member, IEEE*, Álvaro Orellana, Jorge Juliet, *Member, IEEE*, and Roberto Cárdenas, *Senior Member, IEEE*

***Abstract*—This paper presents a new and simple finite-control set model predictive control strategy to reduce the torque ripple in permanent-magnet synchronous machines (PMSMs). The method is based on minimizing a cost function that considers the flux linkage torque harmonics obtained from a discrete-time model of the machine. The power converter switching state that minimizes this cost function is selected and applied during a whole sampling period. Additionally, it is proposed to mitigate the other source of torque ripple, known as cogging-torque, using a feed-forward signal applied to the torque control loop. A hybrid method that uses the output information from an observer and look-up table is presented to obtain a good cogging-torque estimation and thus an accurate mitigation of this disturbance torque at low rotational speed. Experimental results demonstrate the good performance of the torque ripple compensation methods presented in this paper.**

***Index Terms*—Finite-control set model predictive control, permanent-magnet motors, torque control, torque ripple.**

I. Introduction

PERMANENT-MAGNET synchronous machines (PMSMs) are preferentially used for applications in high-performance positioning systems [1], wind energy conversion systems [2], and high-speed servo motors. They offer significant advantages compared with induction machines [2]–[5] such as high dynamic performance, high efficiency due to the absence of excitation windings, reduced copper losses, high torque and power density because of their compact and robust design, and high-power factor through the whole operating range [5]. However, in PMSMs, relative large torque ripple could be produced by spatial harmonics of the air-gap reluctance and magnetic flux linkage, as well as by harmonics in the stator current. Torque ripple leads to acoustic noise and mechanical vibrations [6], the later could reduce the life span of the machine and other mechanical components affixed to the PMSM shaft.

Manuscript received May 27, 2015; revised October 25, 2015 and December 17, 2015; accepted December 20, 2015. Date of publication March 2, 2016; date of current version June 9, 2016. This work was supported by the Chilean Research Council, CONICYT.

A. Mora, A. Orellana, and J. Juliet are with the Department of Electrical Engineering, Universidad Técnica Federico Santa María, Valparaíso 633, Chile (e-mail: andres.mora@usm.cl; alvaro.orellanc@usm.cl; jorge.juliet@usm.cl).

R. Cardenas is with the Department of Electrical Engineering, Universidad de Chile, Santiago 8370451, Chile (e-mail: rcd@ieee.org).

Color versions of one or more of the figures in this paper are available online at http://ieeexplore.ieee.org.

Digital Object Identifier 10.1109/TIE.2016.2536586

Torque ripple of PMSMs is reduced, but not eliminated, by an appropriate magnetic and layout winding design [7], [8]. The control of the machine stator currents could be used to compensate the torque harmonics that cannot be easily eliminated during the design stage. For instance, a conventional field-oriented control (FOC) scheme is proposed in [9] for torque ripple mitigation. However, because of the relatively high-frequency components present in the torque ripple, high-bandwidth currents could be required. In [9] and [10], this is achieved using dead beat controllers. Nevertheless in these publications, the torque ripple is compensated by adding harmonic components in the q-axis stator current reference, and by regulating the d-axis current to zero. Consequently, with $i_d = 0$, maximum torque per ampere (MTPA) cannot be achieved [3], [11] and the machine is no longer operating at the optimal torque.

In recent papers, the use of resonant controllers have also been proposed for the control of PMSMs [4], [12]. Resonant controllers are based on the internal model principle and they can be used to regulate with zero steady-state error signals of sinusoidal nature. For this purpose, one resonant notch is required to regulate a single-frequency component of the harmonic torque. Therefore, to eliminate most of the harmonic distortion, multiresonant controllers are required and the design and digital implementation of such a controller is complex [13]. Moreover, if the control system is implemented in the stationary frame, a tuning mechanism is required to modify the resonant frequencies in real time when variations in the PMSM rotational speed are produced [12].

Recently, the use of finite-control set model predictive control (FCS-MPC) has been proposed for applications involving electrical drives and power converters [14]. With this methodology, a discrete model of the plant and power converter is required to predict the behavior of the system for a particular switching state of the converter. To track references, a cost function which considers the tracking error at each sampling instant is used. The optimal switching action, which minimizes the cost function, is applied to the converter.

As discussed in the literature, FCS-MPC has several advantages. For instance, it is relatively simple to include nonlinearities, constrains, and variables of different nature (electrical or mechanical) in the cost function. The application of FCS-MPC to the control of PMSMs has been discussed in the literature before by using predictive current control [15], [16]. Additionally, in [17] and [18], FCS-MPC is suggested as an alternative to directly regulate the machine torque. The method

is called model predictive direct torque control (MP-DTC), which uses an external speed loop based on a PI controller. However in these papers, control methods to reduce the torque ripple produced by flux linkage harmonic distortion are not addressed. Mitigation of the cogging torque is neither discussed. In [19], a torque predictive control to mitigate the high-frequency torque due to switching effects is presented. However, this paper does not address mitigation of the low-frequency torque pulsations produced by the machine.

Control of the PMSM rotational speed based on FCS-MPC is presented in [20] and [21]. With this approach, the nested control loops typically used in drives are replaced by predictive control system. The results discussed in [20] and [21] show that a high dynamic response can be achieved with this methodology. However, to compensate the load torque an observer has to be implemented, and this may limit the performance of the control system to compensate relatively high-frequency torque components, particularly when the machine is operating at high rotational speed. Moreover, high-bandwidth observers are sensitive to measurement noise, parameter uncertainty, quantization error of the feedback signal, etc.

In this paper, a new control method based on an FCS-MPC controller is presented. The control system is composed of nested loops. The external control loop is used to regulate the PMSM rotational speed using a conventional controller. An internal control loop, based on an FCS-MPC algorithm, directly regulates the torque and minimizes the torque ripple using a cost function based on the full model of the electromagnetic torque, which not only includes the fundamental torque but also the oscillating torque produced by the nonsinusoidal rotor flux distribution. Thereby, a high-bandwidth torque control is implemented and thus, the torque ripple produced by the stator slot harmonics, known as cogging torque [22], can be reduced using a feed-forward compensation term obtained from a cogging torque estimator. Therefore, the proposed torque control reduces the torque-ripple in the PMSM, improving the steady-state performance of the torque control system. Since the proposed control system has similar structure that of the MP-DTC [17], [18], it could be used to achieve MTPA operation which improves the efficiency of anisotropic PMSMs. The methodology required to achieve MTPA by regulating the d-axis current is extensively discussed in [17] and [18]. Therefore, MTPA is considered outside the scope of this work and the interested author is referred elsewhere.

This paper is organized as follows. In Section II, the basis of FCS-MPC are briefly discussed. In Section III, the modeling of the electrical drive, e.g., power converter and PMSM model is analyzed. In Section IV, the proposed methodology to reduce the ripple in the torque is presented. Section V discusses the experimental results that are obtained using a prototype implemented with a 5.4-kW PMSM fed by a two-level voltage source inverter (2L-VSI). Finally, an appraisal of the proposed control method is presented in Section VI.

II. Finite-Control Set Model Predictive Control

In this section, a brief review of FCS-MPC is presented. Further information regarding the applications of this control methodology to power converters and drives is elsewhere [14], [15].

FCS-MPC operates in discrete-time with fixed sampling frequency $f_s = T_s^{-1}$, and uses a discrete-time model of the plant as

$$\boldsymbol{x}_i[k+1] = F(\boldsymbol{x}[k], S_i[k]), \quad \text{for } i = 1, \ldots, n. \tag{1}$$

The vector $\boldsymbol{x}[k]$ groups the m system states to be controlled at time t_k, whereas $S_i[k] \in \mathbb{Z}$ are the n converter switching states, i.e., $\boldsymbol{S} = \{S_1, \ldots, S_n\}$. To select a particular switching state S_i, a decision or cost function, namely G, has to be defined. Usually, the cost function is dependant on the reference values $\boldsymbol{x}^*[k]$ and the predictions $\boldsymbol{x}_i[k+1]$, i.e.,

$$J_i(S_i[k]) = G(\boldsymbol{x}^*[k],\, \boldsymbol{x}_i[k+1]), \quad \text{for } i = 1, \ldots, n. \tag{2}$$

Then, n predictions will lead to n different cost values. Thus, the optimal switching state $S_{\text{op}}[k]$ is defined as that producing the minimum cost. A typical example for G is the quadratic error between the references and predictions

$$J_i(S_i[k]) = \boldsymbol{e}_i[k]^T \left[\mathbf{W}\right] \boldsymbol{e}_i[k] = \sum\nolimits_{j=1}^{m} \lambda_j \, e_{ji}^2 \tag{3}$$

where $\boldsymbol{e}_i[k] = \boldsymbol{x}^*[k] - \boldsymbol{x}_i[k+1]$, $\mathbf{W} = \text{diag}\{\lambda_1, \ldots, \lambda_m\}$, and $\lambda_i \geq 0$ are weighting factors, which are used to tune the importance of each variable in relation to the other ones.

The ideal theoretical case in which the variables can be measured, the cost function evaluated, the optimal switching pattern calculated, and the power converter controlled instantly at time t_k is not realizable in real-time applications. However, this problem can be overcome when a two-step ahead prediction is considered in which the switching state to be applied in the following sampling time $S[k+1]$ is determined. Thus, the effect of this control action will be observed only at the instant t_{k+2}. For this delay, it is necessary to predict not only the value of the variables to be controlled at t_{k+2} but also to estimate their values at t_{k+1}. Once determined the first prediction of the states $\boldsymbol{x}[k+1]$, the FCS-MPC algorithm is performed for the n possible switching states, leading to one optimal selection $S_{\text{op}}[k+1]$, which is applied from instant t_{k+1} to t_{k+2}.

III. Description of the Drive

A. Model of the Converter

The representation of a 2L-VSI is shown in Fig. 1(a). This converter is composed by a dc-voltage source and three half-bridge units in the inverter stage. Each phase can be connected to the positive or negative terminal using the power switches of the corresponding half-bridge. The inverter switching states are determined by the gating signals S_x. For the 2L-VSI shown in Fig. 1(a), there are $2^3 = 8$ different switching states. Using a vector notation, a given switching state can be written as

$$\boldsymbol{S} = \frac{2}{3}\left(S_a + \boldsymbol{a}\, S_b + \boldsymbol{a}^2\, S_c\right), \quad \boldsymbol{a} = e^{j\frac{2\pi}{3}} \tag{4}$$

which are represented in Fig. 1(b). Finally, the output voltage vector can be calculated as $\boldsymbol{u}_s^{(S)} = u_{\text{dc}}\, \boldsymbol{S}$, where u_{dc} is the dc-link voltage, and the superscript $^{(S)}$ denotes α–β coordinates referred to the stationary frame.

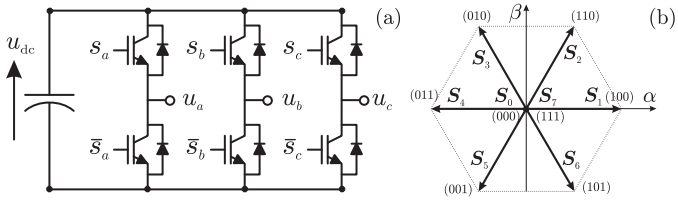

Fig. 1. 2L-VSI: (a) Topology. (b) voltage vectors in α–β plane.

B. Dynamic Model of the PMSM

The control scheme is based on the dynamic model of the PMSM referred to a rotor-fixed reference frame orientated along the rotor flux [9]. Using the stator currents $\boldsymbol{i}_s = \begin{bmatrix} i_d & i_q \end{bmatrix}^T$, the following state equations can be used to describe the dynamic of the PMSM:

$$\frac{d\boldsymbol{i}_s}{dt} = -\mathbf{A}_c(\omega)\,\boldsymbol{i}_s + \mathbf{B}_c\,[\boldsymbol{u}_s - \boldsymbol{u}_i] \tag{5}$$

$$\mathbf{A}_c(\omega) = \begin{bmatrix} \frac{R_s}{L_d} & -\omega\frac{L_q}{L_d} \\ \omega\frac{L_d}{L_q} & \frac{R_s}{L_q} \end{bmatrix}, \quad \mathbf{B}_c = \begin{bmatrix} \frac{1}{L_d} & 0 \\ 0 & \frac{1}{L_q} \end{bmatrix} \tag{6}$$

where R_s is the stator winding resistance, L_d and L_q are d–q axis stator self-inductances, $\omega = d\theta/dt$ is the rotor speed, and θ is the rotor position.

In (5), $\boldsymbol{u}_s$ is the stator voltage vector (in rotor coordinates) applied by the converter and $\boldsymbol{u}_i$ is the machine back-EMF, which is produced by the stator flux linkage due to the rotor magnets and can be obtained as

$$\boldsymbol{u}_i = \mathbf{J}\omega\boldsymbol{\Phi}(\theta), \quad \mathbf{J} = \begin{bmatrix} 0 & -1 \\ 1 & 0 \end{bmatrix} \tag{7}$$

where

$$\boldsymbol{\Phi}(\theta) = \begin{bmatrix} \phi_d(\theta) \\ \phi_q(\theta) \end{bmatrix} = \begin{bmatrix} \Phi_F + \phi_{dh}(\theta) \\ \phi_{qh}(\theta) \end{bmatrix} \tag{8}$$

is a function of the flux linkage, whose harmonics components in the d- and q-axis are ϕ_{dh} and ϕ_{qh}, respectively [9]. Notice that $\boldsymbol{\Phi}(\theta)$ is equal to the magnitude of the fundamental rotor flux Φ_F only when the permanent-magnet flux linkage describes a perfectly circular trajectory in the α–β plane.

C. Oscillations in the Electromagnetic Torque

1) Flux Linkage Harmonics: The electromagnetic torque can be separated into excitation torque, reluctance torque, and cogging torque. The former is obtained using [9]

$$T_e = \frac{3}{2}\frac{p}{\omega}\left(u_{id}\,i_d + u_{iq}\,i_q\right) \tag{9}$$

where p is the number of pole pairs. By replacing (7) and (8) into the above equation, the excitation torque is calculated as

$$T_e = \frac{3}{2}p\,\left(\Phi_F\,i_q\right) + \frac{3}{2}p\,\left(\phi_{dh}(\theta)\,i_q - \phi_{qh}(\theta)\,i_d\right). \tag{10}$$

The first term at the right-hand side is the fundamental torque, which is constant if i_q is constant. The second term at the right-hand side of (10) may produce harmonic components in the torque. These oscillations are produced by the flux harmonics components ϕ_{dh} and ϕ_{qh} interacting with the spatial current distribution $\boldsymbol{i}_s$.

2) Slotting Torque: In the PMSM, reluctance torque and cogging torque can be produced. The former is calculated as

$$T_R(\boldsymbol{i}_s) = \frac{3}{2}p\,(L_d - L_q)\,i_d\,i_q. \tag{11}$$

Therefore, the reluctance torque is zero when the rotor surface is magnetically isotropic and $L_d = L_q$. On the other hand, the cogging torque is generated by the interaction of the permanent-magnet flux density and angular variations in the air-gap reluctance. Then, the cogging torque is a periodic function of the angular position in mechanical coordinates ($\theta_m = \theta/p$), and can be represented by a Fourier series [22]

$$T_{\text{cogg}}(\theta_m) = \sum\nolimits_{k=1}^{\infty} T_{mk}\sin\left(m\,k\theta_m\right) \tag{12}$$

where m is the least common multiple of stator slots N_s and the number of poles $2p$. In (12), T_{mk} represents the Fourier coefficients.

D. Discrete-Time Model of PMSM

The discrete model of PMSM is used to predict the future value of the variables to be controlled. Since the main goal of the control scheme is to regulate the fundamental torque T_0 and also to compensate the oscillatory torque due to flux linkage harmonics T_Φ, the full model of the electromagnetic torque has to be included. This model is based on (10) and (11) as follows:

$$T[k] = \frac{3}{2}p\underbrace{\left(\Phi_F\,i_q[k] + (L_d - L_q)i_d[k]\,i_q[k]\right)}_{T_0} + \frac{3}{2}p\underbrace{\left(\phi_{dh}[k]\,i_q[k] - \phi_{qh}[k]\,i_d[k]\right)}_{T_\Phi}. \tag{13}$$

Thereby, the prediction of the torque $T[k+1]$ is calculated using (13). However, to achieve this is necessary to predict $\boldsymbol{i}_s[k+1]$, as well as $\boldsymbol{\Phi}[k+1]$. Using discrete-time versions of (5) and (6), $\boldsymbol{i}_s[k+1]$ is calculated as

$$\boldsymbol{i}_s[k+1] = \mathbf{A}_d(\omega_k)\boldsymbol{i}_s[k] + \mathbf{B}_d(\omega_k)\,[\boldsymbol{u}_s[k] - \mathbf{J}\omega_k\boldsymbol{\Phi}[k]] \tag{14}$$

where the discrete-time matrices are calculated using

$$\mathbf{A}_d(\omega_k) = \mathrm{e}^{-\mathbf{A}_c(\omega_k)\,T_s} \tag{15}$$

$$\mathbf{B}_d(\omega_k) = \mathbf{A}_c(\omega_k)^{-1}\cdot\left[\mathbf{I} - \mathrm{e}^{-\mathbf{A}_c(\omega_k)\,T_s}\right]\cdot\mathbf{B}_c. \tag{16}$$

To obtain a discrete representation of the time-varying matrices [see (15) and (16)], the use of a good methodology is desirable. The conventional method to obtain a discrete representation of the system is to use an Euler approximation, which represents a first-order series expansion. Since in a typical PMSM the stator time constant is relatively small, a [1/1]-Padé approximation [23] is preferred in this work to calculate (15). Thereby, a smaller prediction error and better performance in the FCS-MPC is obtained with the following discrete-time matrices:

$$\mathbf{A}_d(\omega_k) = \left[\mathbf{I} - \tfrac{T_s}{2}\mathbf{A}_c(\omega_k)\right]\cdot\left[\mathbf{I} + \tfrac{T_s}{2}\mathbf{A}_c(\omega_k)\right]^{-1} \tag{17}$$

$$\mathbf{B}_d(\omega_k) = \left[\mathbf{I} + \tfrac{T_s}{2}\mathbf{A}_c(\omega_k)\right]^{-1}\cdot T_s\,\mathbf{B}_c. \tag{18}$$

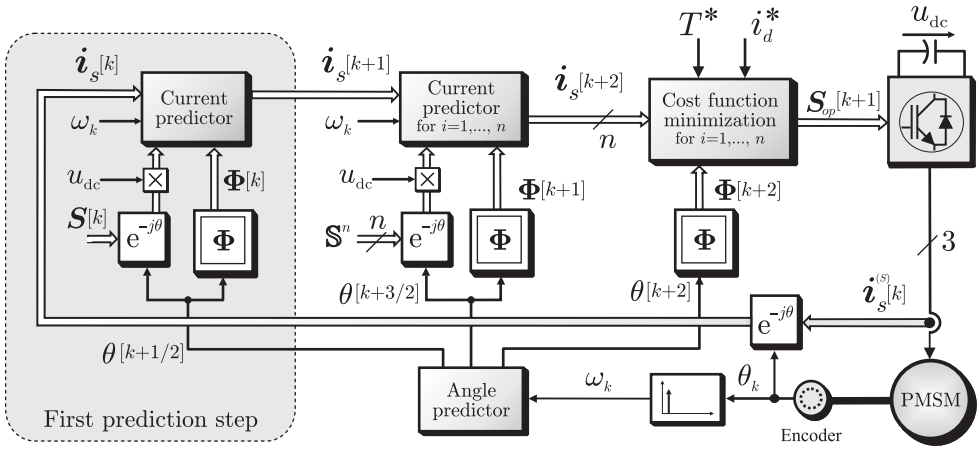

Fig. 2. Proposed MPTC scheme for the PMSM.

On the other hand, in (14), the speed ω_k (at instant t_k) is assumed constant during the whole sampling period. However, the rotor position angle is not constant and the variation in the the stator voltage vector $\boldsymbol{u}_s$ is calculated as

$$\boldsymbol{u}_s = u_{\rm dc}\boldsymbol{S}\,\mathrm{e}^{-j\theta(t)} \tag{19}$$

where the rotor position is

$$\theta(t) = \omega_k(t - t_k) + \theta_k, \quad t_k \le t < t_k + T_s. \tag{20}$$

To overcome this, the mean value of $\boldsymbol{u}_s$ is considered as an input voltage at t_k, i.e.

$$\begin{aligned}\boldsymbol{u}_s[k] &= \frac{1}{T_s}\int_{t_k}^{t_k+T_s} u_{\rm dc}\boldsymbol{S}[k]\mathrm{e}^{-j\theta(\tau)}d\tau \\ &= \boldsymbol{u}_s^{(S)}[k]\mathrm{e}^{-j\theta_k}\left(\frac{\mathrm{e}^{-j\omega_k T_s}-1}{-j\omega_k T_s}\right) \\ &\simeq \boldsymbol{u}_s^{(S)}[k]\mathrm{e}^{-j\left(\theta_k+\frac{\omega_k T_s}{2}\right)}.\end{aligned} \tag{21}$$

Then, the stator voltage vector in (21) represents a better approximation than that conventionally used, namely $\boldsymbol{u}_s[k] = \boldsymbol{u}_s^{(S)}[k]\mathrm{e}^{-j\theta_k}$ (see [15]–[17]), particularly when the rotor speed is high. From (21) is concluded that the stator voltage vector has to be evaluated at the rotor position angle obtained at the middle of the sampling time

$$\theta[k+1/2] = \theta_k + \tfrac{T_s}{2}\,\omega_k. \tag{22}$$

Therefore, to determinate $\boldsymbol{i}_s[k+1]$ in (14), the inputs at the time t_k are calculated using

$$\begin{aligned}\boldsymbol{u}_s[k] &= u_{\rm dc}\boldsymbol{S}[k]\,\mathrm{e}^{-j\theta[k+1/2]} \\ \boldsymbol{\Phi}[k] &= \boldsymbol{\Phi}(\theta[k+1/2]).\end{aligned} \tag{23}$$

IV. Torque Ripple Compensation With FS-MPC

A. Model Predictive Torque Control (MPTC)

For the conventional control of PMSMs, the torque producing current (i_q) is regulated using a current control system implemented in rotor coordinates. However, the regulation of the harmonic current i_{qh} is limited due to the inherent bandwidth of the controller. Although high-bandwidth controllers can be implemented (e.g., dead-beat and conventional FCS-MPC [15], [16]), some complex real-time calculations have to be realized in order to obtain the required i_{qh} current (e.g., see [9], [10]). As an alternative and simpler solution in this paper, it is proposed to reduce the torque ripple by adding the oscillatory torque prediction of T_Φ to the cost function of the FCS-MPC scheme. Thereby, the proposed cost function is

$$J = \left(T^* - (T_0 + \lambda_h\, T_\Phi)\right)^2 + \lambda_d\,\left(i_d^* - i_d[k+2]\right)^2 + \hat{f}(\boldsymbol{S}) \tag{24}$$

where λ_h and λ_d are the weighting factors, and $\hat{f}(\boldsymbol{S})$ is the function that penalizes the switching states producing overcurrent in the stator windings [15]. On the other hand, the torque predictions are calculated using

$$\begin{aligned}T_0 &= \frac{3}{2}p\left(\Phi_F\, i_q[k+2] + (L_d - L_q) i_d[k+2]\, i_q[k+2]\right) \\ T_\Phi &= \frac{3}{2}p\left(\phi_{dh}[k+2]\, i_q[k+2] - \phi_{qh}[k+2]\, i_d[k+2]\right).\end{aligned} \tag{25}$$

In the proposed control strategy (MPTC), an additional term $\lambda_h\, T_\Phi$ in the cost function is added to mitigate the torque-ripple produced by the stator flux linkage harmonics. Notice that the conventional MPTC uses $\lambda_h = 0$ (see [17] and [18]). Therefore, only the fundamental torque is controlled.

The proposed MPTC scheme is shown in Fig. 2. As depicted in this control diagram, the values of $\boldsymbol{\Phi}$ are calculated directly in rotor coordinates, whereas the switching state vectors $\boldsymbol{S} \in \mathbb{S}^n$ are transformed to rotor coordinates to obtain the input voltage vector referred to the rotating dq frame. Thus, the n future current values $\boldsymbol{i}_s(\boldsymbol{S})[k+2]$ are computed by the current predictor (14), with the following inputs:

$$\begin{aligned}\boldsymbol{u}_{s,i}[k+1] &= u_{\rm dc}\,\boldsymbol{S}_i\,\mathrm{e}^{-j\theta[k+3/2]}, \quad i = 1,\ldots,n \\ \boldsymbol{\Phi}[k+1] &= \boldsymbol{\Phi}\left(\theta_k + 3/2\,\omega_k T_s\right).\end{aligned} \tag{26}$$

To overcome the intrinsic delay of the power converter and digital systems (see Section II), the optimal switching state

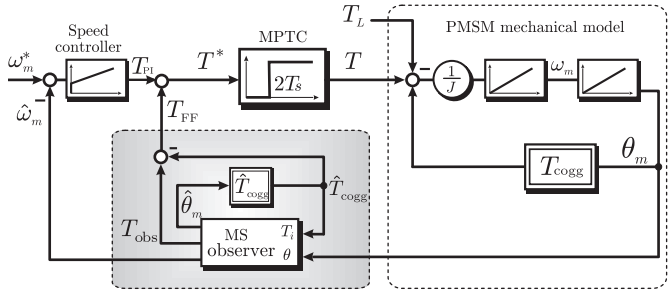

Fig. 3. Speed control scheme with hybrid cogging torque compensation.

calculated in the previous sampling time $\boldsymbol{S}[k]$ is applied to determinate $\boldsymbol{i}_s[k+1]$, which represents the first current prediction. In this case, the space vectors $\boldsymbol{u}_s$ and $\boldsymbol{\Phi}$ are obtained by (23) as shown in the shaded box at the left of Fig. 2. Moreover, as also shown in Fig. 2, the current $\boldsymbol{i}_s[k+1]$ and the flux $\boldsymbol{\Phi}[k+1]$ are used to obtain n predictions (one for each switching state $\boldsymbol{S} \in \mathbb{S}^n$) of the stator current $\boldsymbol{i}_s[k+2]$.

Once the n-predictions of the stator current at t_{k+2} are obtained, the n-costs are calculated by using (24), which also requires the function $\boldsymbol{\Phi}$ at instant t_{k+2}. Finally, the switching state that minimizes the cost function is the problem solution and the optimal control action to apply at t_{k+1}, i.e., $\boldsymbol{S}_{\text{op}}[k+1]$.

B. Cogging Torque Compensation

In this paper, compensation of the cogging torque is proposed using a methodology based on a state observer and a feed-forward compensating signal (see Fig. 3). As discussed previously, in this work, two nested control systems are used, where the inner torque control loop is based on a model predictive controller and the external control loop is based on a conventional PI controller. Because of the relatively low bandwidth of the speed control system, the external control loop can hardly compensate the cogging torque and a better dynamic response can be obtained if a feed-forward compensation term is applied to the inner control loop.

In Fig. 3, the proposed cogging torque compensation scheme is shown, where MPTC is modeled as a $2T_s$ delay, whereas the cogging torque compensation is achieved using a feed-forward signal T_{FF}. This signal is obtained using an observer and a look-up table, where information about the cogging torque, as a function of the rotor position angle [i.e., $\hat{T}_{\text{cogg}}(\theta_m)$] is stored.

The mechanical observer used in this paper is based on the work discussed in [24]. This closed-loop observer (see Fig. 4) requires the quantized rotor position θ_m and the estimation of disturbances as inputs. The outputs are the estimation of the mechanical speed $\hat{\omega}_m$, the smoothed rotor position $\hat{\theta}_m$, and the observed torque $\hat{T}_{\text{obs}}$, whose transfer function is

$$\hat{T}_{\text{obs}} = -\frac{K_3(T + T_{\text{cogg}} - T_L - T_i)}{Js^3 + JK_1s^2 + K_2s + K_3}. \tag{27}$$

Therefore, the dynamic performance and the bandwidth of this estimator is dependent of the gains K_1, K_2, and K_3. Notice that the observed torque $\hat{T}_{\text{obs}}$ is also dependent on the command input T_i as a feed-forward signal.

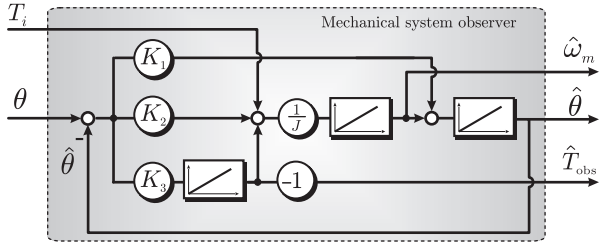

Fig. 4. Closed-loop MS observer [24].

Using the look-up table and the mechanical observer, three cogging torque compensation methods can be implemented. The look-up table method, the observer method, and a hybrid method which is a combination of the two mentioned above. When the compensation system is operating with the look-up table method, the observer is ignored and $T_{\text{FF}} = \hat{T}_{\text{cogg}}$.

In the observer compensation method, $T_i = 0$ (see Fig. 4) and, within the observer bandwidth, the observed torque is $\hat{T}_{\text{obs}} = -T_{\text{cogg}} + T_L - T$ whose value is used as the feed-forward signal T_{FF}. Instead, in the hybrid method, the command input is $T_i = \hat{T}_{\text{cogg}}$ and the observer output is

$$\hat{T}_{\text{obs}} = T_L - T - T_{\text{cogg}} + \hat{T}_{\text{cogg}}. \tag{28}$$

Thereby, in steady state, the observed torque is the residual component that is not previously measured in the cogging torque table $\hat{T}_{\text{cogg}}$. Moreover, within the bandwidth of the mechanical observer depicted in Fig. 4, the hybrid method uses the observer cogging torque $\hat{T}_{\text{obs}}$ and converges to the look-up table cogging torque $\hat{T}_{\text{cogg}}$ value when the frequency of the signal is close or higher than the mechanical observer bandwidth. Notice that for both cogging torque estimators based on the observer depicted in Fig. 4, not only the cogging torque is compensated but also the error between the load and electromagnetic torque. This improves the control system dynamic response to load impacts.

Finally, the cogging torque as a function of the rotor position is experimentally estimated by operating the machine in speed control mode and no-load condition. Therefore, the effect of $\boldsymbol{\Phi}(\theta)$ in the electromagnetic torque is neglected and oscillations in the torque are produced by the cogging torque. Moreover, if the speed reference is very low, the torque harmonic frequency is within the speed controller bandwidth. Thus, the oscillating torque, which is assumed equal to the slot torque $\hat{T}_{\text{cogg}}(\theta)$, can be compensated by the speed controller output signal T_{PI} as shown in Fig. 3. Notice that for this test the signal T_{FF} of Fig. 3 is disabled and the value of $\hat{T}_{\text{cogg}}$ is estimated from the output of the speed controller.

V. Experimental Validation

This section presents the experimental results obtained for the proposed control methodology. The test machine is a 5.4-kW Servomotor Brushless with 10 poles and 12 slots [see Fig. 5(a)], whose main parameters are detailed in Table I.

The permanent-magnet motor is loaded by mechanically coupling to the shaft a 5.5-kW induction motor [see Fig. 5(b)], controlled by a commercial servo drive [see Fig. 6(d)].

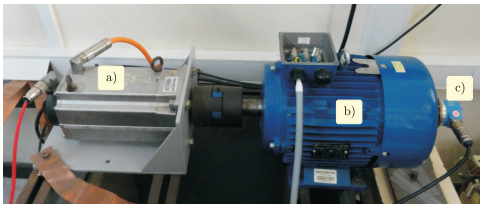

Fig. 5. Machines setup. (a) PMSM. (b) Induction machine. (c) Encoder.

TABLE I
PMSM PARAMETERS

P_R	5400	W	R_s	0.750	Ω
U_R	230	V	L_d	2.490	mH
ω_R	1450	rpm	L_q	3.075	mH
T_R	35.6	Nm	Φ_F	0.215	Wb
I_R	16.3	A_{rms}	K_T	2.280	Nm/A_{rms}
Back-EMF @ 1000 rpm	138	V_{rms}	J	0.041	kgm^2

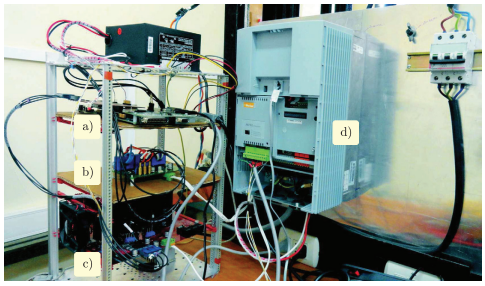

Fig. 6. Laboratory setup. (a) DSP+FPGA+FO interface. (b) Current sensor. (c) 2L-VSI. (d) Induction machine converter.

The control algorithms are implemented in a TMS320C6713 DSP [see Fig. 6(a)], which is coupled to a XC3S400 FPGA. This FPGA board controls the A/D converters, encoder reading, and IGBT gate switching signals. Optical fiber is used to interface the 2L-VSI with the FPGA board. The sampling frequency used is 15 kHz.

For the selection of the weighting factors λ_h and λ_d utilized in the cost function of (24), the Branch and Bound algorithm (BBA) reported in [15] and [25] has been used in this work. The first step to apply this methodology is to normalize the cost function using per-unit analysis, i.e., referring the torque and current respect to their nominal values [25] (base current: $I_B = \sqrt{2}I_R = 23.1$ A, base torque: $T_B = T_R = 35.6$ Nm). In order to give the same relevance to the harmonic torque T_Φ and the fundamental torque T_0, the first weighting factor is set to $\lambda_h = 1$. Thereafter, the value of λ_d was obtained using the branch and bound procedure considering as figures of merit the torque ripple and the effective (rms) error in the d-axis current respect to the reference $i_d^* = 0$ [see (24)]. Finally, the weighting factors were selected as $\lambda_h = 1$ and $\lambda_d = 0.5$.

Additional information about the BBA and the selection of figures of merit, to evaluate the performance achieved by the weighting factors, is available in [15] and [25].

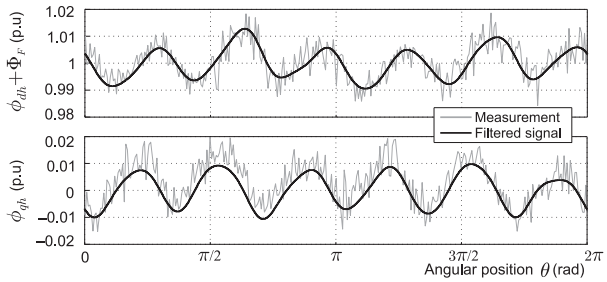

Fig. 7. Two-axes of the flux linkage harmonics function $\mathbf{\Phi}(\theta)$.

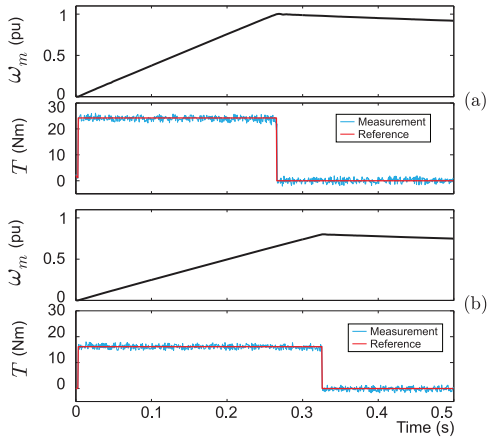

Fig. 8. Acceleration test. (a) $T^* = 24.2$ Nm. (b) $T^* = 16.1$ Nm.

A. Compensation of the Flux Linkage Harmonics

To implement the proposed MPTC, it is necessary to estimate the complex function $\mathbf{\Phi}(\theta)$ [9]. In this paper, $\mathbf{\Phi}(\theta)$ is experimentally estimated by operating the machine at rated speed as an unload generator ($\boldsymbol{i}_s = 0$). Under this operating condition, the induced voltage satisfies (7), then

$$\mathbf{\Phi}(\theta) = \mathbf{J}^{-1}\frac{\boldsymbol{u}_i}{\omega_R}, \quad \boldsymbol{u}_i = \mathbf{T}(\theta)\begin{bmatrix}\frac{2}{3}u_{ac} - \frac{1}{3}u_{bc} \\ \frac{\sqrt{3}}{3}u_{bc}\end{bmatrix} \tag{29}$$

where u_{ac} and u_{bc} are the measured line-to-line voltages, and $\mathbf{T}(\theta)$ is the Park transformation. The matrix $\mathbf{J}$ is defined in (7).

The two-axes components (in p.u. of the fundamental d-axis flux Φ_F) are shown in Fig. 7. Notice that the sixth-order harmonic with an amplitude of about 1% of Φ_F.

To demonstrate the performance of the control scheme, the tested PMSM motor operates in torque control mode and its electromagnetic torque is estimated from terminal quantities through (13). So the estimation comprises flux linkage harmonics, but excludes slot harmonics. Because of simplicity, the d-axis current is regulated to zero.

In Fig. 8(a), the performance of the proposed MPTC is shown for step changes in the reference torque. In $t = 0$ s, a torque reference of 24.2 Nm (with $i_{sq} = 15$ A) is used and the machine accelerates to about 1500 rpm, later the reference is set again to zero. The same maneuver was carried out with a torque reference of 16.1 Nm (with $i_{sq} = 10$ A) [see Fig. 8(b)]. As shown in these torque waveforms, a good tracking (without overshoot) of the torque reference is achieved by the MPTC.

Compensation of flux linkage harmonics is demonstrated in Fig. 9 with a torque reference of 24.2 Nm applied to the shaft

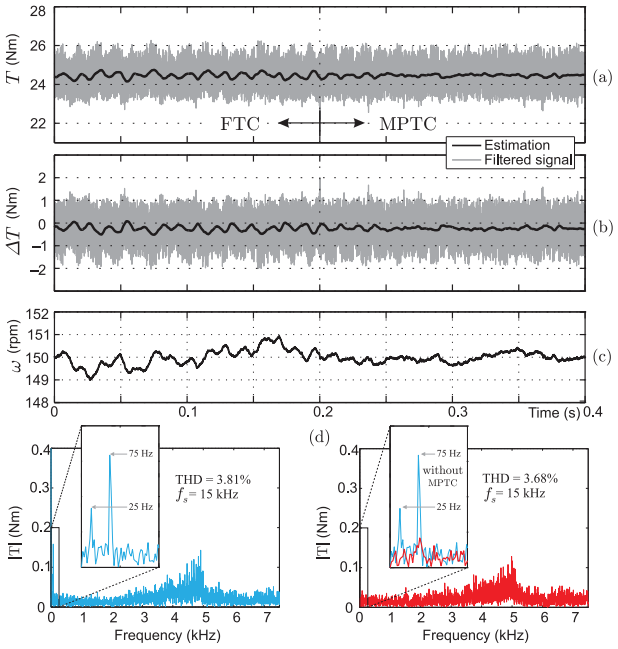

Fig. 9. Compensation of flux linkage harmonics torque at 150 rpm. (a) Torque. (b) Torque tracking error. (c) Speed. (d) Comparison of harmonic spectrum.

while the PMSM is operating at 150 rpm. The slot harmonic torque compensation is enabled during this test to eliminate the cogging torque. Fig. 9(a) shows the performance comparison between a control scheme where only the fundamental torque is controlled (FTC) (where $\lambda_h = 0$) and the predictive torque control proposed in this paper, which is labelled MPTC in Fig. 9. In order to eliminate the effects of the switching frequency in the waveform shown in Fig. 9(a), the torque has been filtered (cutoff frequency 200 Hz). As concluded from Fig. 9(a), the performance of the MPTC is better than that of the FTC to compensate the torque oscillations. On the other hand, the torque tracking error [see Fig. 9(b)] shows a reduced nonzero steady-state error, which is one of the feature of the conventional FCS-MPC [26]. However, this nonzero tracking error is presented with both FTC and MPTC schemes.

The speed oscillation is reduced considerably as shown in Fig. 9(c). Notice that additional low-frequency speed fluctuations arise due to small misalignments in the shaft, which are produced under both control schemes.

Additionally, the comparison of both Fourier spectra is shown in Fig. 9(b) and (c). Two low-frequency components, of 25 and 75 Hz, are present in the FTC performance. These components are almost eliminated by the proposed MPTC. Notice that both frequency components are torque harmonic of second- and sixth-order, respectively. This is in broad agreement with the spectrum of $\mathbf{\Phi}(\theta)$ [see Fig. 7].

The machine torque current corresponding to the experimental test of Fig. 9 is shown in Fig. 10(a). As discussed previously, because of the space harmonics in the flux linkage, the injection of harmonics in the q-axis component of $\boldsymbol{i}_s$ is required to compensate the torque oscillations. This is automatically achieved by the proposed MPTC algorithm, but not with the FTC scheme, which sets an almost constant i_q [see Fig. 10(a)].

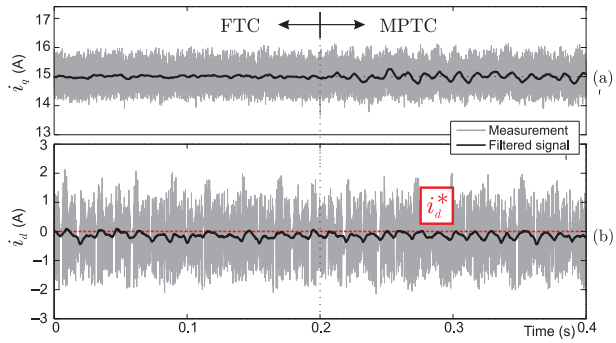

Fig. 10. Compensation of flux linkage harmonics torque. (a) i_q. (b) i_d.

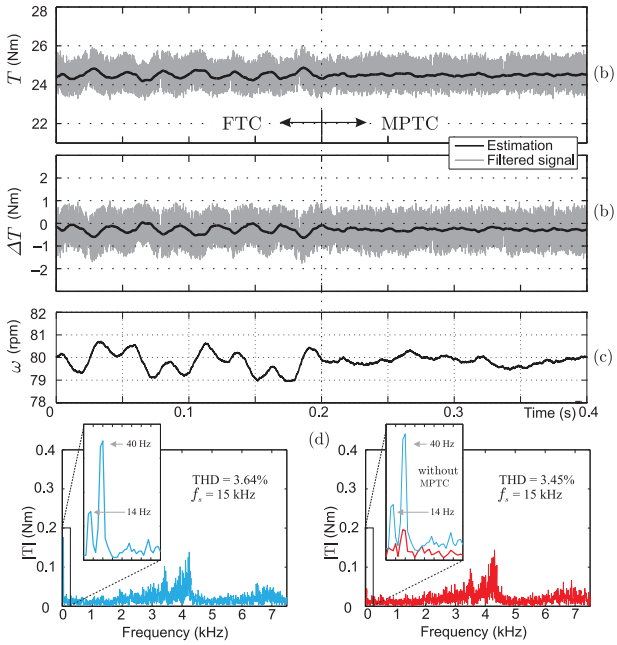

Fig. 11. Compensation of flux linkage harmonics torque at 80 rpm. (a) Torque. (b) Torque tracking error. (c) Speed. (d) Comparison of harmonic spectrum.

The i_d current is controlled to zero with a reduced steady-state tracking error as shown in Fig. 10(b).

Regarding harmful effects of the compensation, injection of current harmonics would eventually increase the winding losses. In this case, the copper losses are increased in about 0.015%, which is negligible. On the other hand, during the experimental validation of the proposed control methodologies, high-intensity audible noise was not produced by the injection of the compensating currents.

Additionally, in order to demonstrate the good performance of the MPTC at low rotational speeds, another test at lower speed (80 rpm) was carried out and the results are shown in Fig. 11. The effect of the compensation is depicted in Fig. 11, where oscillation in the electromagnetic torque and the mechanical speed are clearly reduced. This experiment shows that similar results were obtained at 150 rpm, where good mitigation of torque and speed oscillations are achieved with a small steady-state torque tracking error [see Fig. 11(b)]. Finally, the comparison of speed harmonic spectrum is demonstrated for both tests in Fig. 12. When the compensation is not enabled that

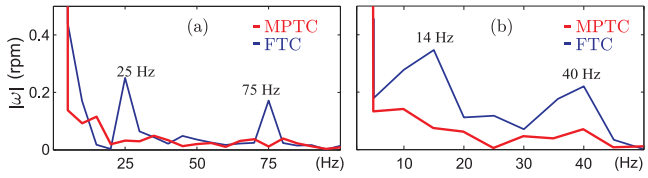

Fig. 12. Comparison of speed harmonic spectrum considering/nonconsidering MPTC. (a) 150 rpm. (b) 80 rpm.

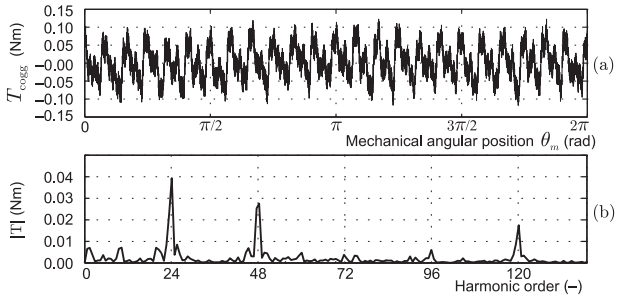

Fig. 13. T_{cogg} estimation. (a) Measurement. (b) Harmonic spectrum.

the torque harmonic is reflected in the speed. However, when the compensation is activated that the two peaks shown in the speed harmonic spectrum have negligible amplitudes.

B. Cogging Torque Compensation

In this section, experimental results corresponding to the three cogging torque compensation methods are discussed. These results were obtained operating the PMSM motor in speed control mode with a speed reference of 30 rpm and no-load condition to eliminate the influence of flux linkage harmonics in the electromagnetic torque. Therefore, the torque ripple is only produced by the cogging torque.

Fig. 13(a) shows the spectral estimation of the machine cogging torque obtained experimentally; there are 24 pulsations per mechanical revolution, which is a multiple of the number of slots. In machines with a fractional number of slots per pole, as in this case ($N_s/2p = 1.2$), the fundamental frequency of the overall cogging torque is an integer multiple of the number of slots [22]. Therefore, the order of the fundamental cogging torque is $h\,N_s$, coinciding with the harmonic spectrum in Fig. 13(b) where $h = 2$.

The effect of cogging torque compensation using the look-up table is demonstrated in Fig. 14. The torque reference, obtained from the speed controller and the feed-forward term $\hat{T}_{\text{cogg}}$, obtained from the look-up table, are shown in Fig. 14(a). Notice that a good mitigation of the high-frequency components of ω_m can be achieved by this offline method as shown in Fig. 14(b).

The performance of the method based on the observer method is shown in the first two seconds of Fig. 15(a). As shown in this graphic, the compensation achieved by the observer method is slightly better than that obtained by the look-up table method shown in Fig. 14.

The hybrid method (look-up table + observer) performance is shown in the last two seconds of Fig. 15(b). As discussed in Section IV-B, the methodology to obtain the compensation signal T_{FF} is depicted in Fig. 3 (see the shaded box in that

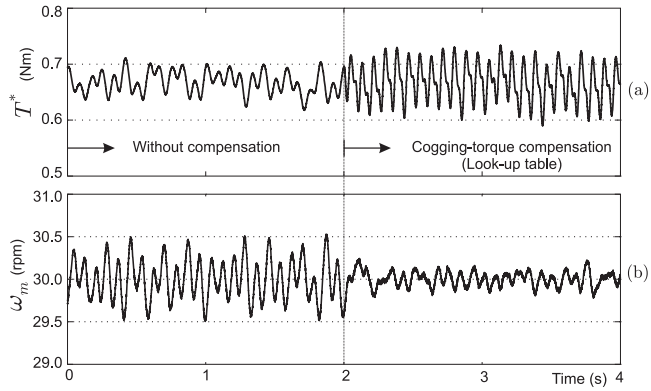

Fig. 14. Compensation of slot harmonics torque by look-up table $\hat{T}_{\text{cogg}}(\hat{\theta})$. (a) Electromagnetic torque reference T^*. (b) Mechanical speed ω_m.

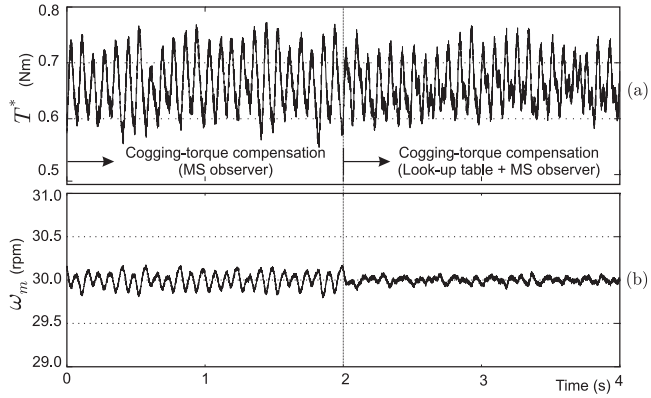

Fig. 15. Performance comparison of slot torque compensation. (a) Electromagnetic torque reference T^*. (b) Mechanical speed ω_m.

figure) with $T_i = \hat{T}_{\text{cogg}}$. From the speed waveforms shown in Figs. 14(b) and 15(b), it is concluded that the hybrid compensation method has the best performance for slot torque compensation.

Finally, as shown in the torque reference waveforms [see Figs. 14(a) and 15(a)] for the three compensation methods, each compensation signal has a predominant harmonic of 12 Hz, which represents the 24th-order component analyzed in the harmonic spectrum of Fig. 13(b).

VI. Conclusion

In this paper, an MPTC strategy has been discussed which is based on the discrete-time state-space model of the PMSM. A torque equation that includes the oscillatory torque produced by spatial harmonics in the permanent-magnet field has been developed. The torque oscillations produced by the nonsinusoidal flux linkage is minimized by using an additional term in the cost function of the FS-MPC scheme. The methodology proposed in this paper produces an automatic injection of harmonics in the q-axis current, which significantly reduces the ripple in the electromagnetic torque.

The torque ripple produced by the stator slot harmonics is reduced through feed-forward compensation signals, which are calculated using three methods. According with the results

presented in this paper, the hybrid method proposed in this paper produces the best compensation of the cogging torque.

REFERENCES

[1] G. Wang, T. Li, G. Zhang, X. Gui, and D. Xu, "Position estimation error reduction using recursive-least-square adaptive filter for model-based sensorless interior permanent-magnet synchronous motor drives," *IEEE Trans. Ind. Electron.*, vol. 61, no. 9, pp. 5115–5125, Sep. 2014.

[2] M. Liserre, R. Cardenas, M. Molinas, and J. Rodriguez, "Overview of multi-mw wind turbines and wind parks," *IEEE Trans. Ind. Electron.*, vol. 58, no. 4, pp. 1081–1095, Apr. 2011.

[3] R. Ni, D. Xu, G. Wang, L. Ding, G. Zhang, and L. Qu, "Maximum efficiency per ampere control of permanent-magnet synchronous machines," *IEEE Trans. Ind. Electron.*, vol. 62, no. 4, pp. 2135–2143, Apr. 2015.

[4] C. Xia, B. Ji, and Y. Yan, "Smooth speed control for low-speed high-torque permanent-magnet synchronous motor using proportional-integral resonant controller," *IEEE Trans. Ind. Electron.*, vol. 62, no. 4, pp. 2123–2134, Apr. 2015.

[5] M. Melfi, S. Evon, and R. McElveen, "Induction versus permanent magnet motors," *IEEE Ind. Appl. Mag.*, vol. 15, no. 6, pp. 28–35, Nov. 2009.

[6] A. Gebregergis, M. Chowdhury, M. Islam, and T. Sebastian, "Modeling of permanent-magnet synchronous machine including torque ripple effects," *IEEE Trans. Ind. Electron.*, vol. 51, no. 1, pp. 232–239, Jan. 2015.

[7] K.-C. Kim, "A novel method for minimization of cogging torque and torque ripple for interior permanent magnet synchronous motor," *IEEE Trans. Magn.*, vol. 50, no. 2, pp. 793–796, Feb. 2014.

[8] W. Fei and P.-K. Luk, "Torque ripple reduction of a direct-drive permanent-magnet synchronous machine by material-efficient axial pole pairing," *IEEE Trans. Ind. Electron.*, vol. 59, no. 6, pp. 2601–2611, Jun. 2012.

[9] L. Springob and J. Holtz, "High-bandwidth current control for torque-ripple compensation in pm synchronous machines," *IEEE Trans. Ind. Electron.*, vol. 45, no. 5, pp. 713–721, Oct. 1998.

[10] H. Jia, M. Cheng, W. Hua, Z. Yang, and Y. Zhang, "Compensation of cogging torque for flux-switching permanent magnet motor based on current harmonics injection," in *Proc. IEEE Int. Elect. Mach. Drives Conf. (IEMDC'09)*, May 2009.

[11] M. H. Rashid, *Power Electronics Handbook*. San Diego, CA, USA: Academic, 2001.

[12] R. Cardenas, E. Espina, J. Clare, and W. Patrick W., "Self-tuning resonant control of a 7-leg back-to-back converter for interfacing variable speed generators to 4-wire loads," *IEEE Trans. Ind. Electron.*, vol. 62, no. 7, pp. 4618–4629, Jul. 2015.

[13] A. Hasanzadeh, C. Edrington, B. Maghsoudlou, F. Fleming, and H. Mokhtari, "Multi-loop linear resonant voltage source inverter controller design for distorted loads using the linear quadratic regulator method," *IET Power Electron.*, vol. 5, no. 6, pp. 841–851, Jul. 2012.

[14] J. Rodriguez *et al.*, "State of the art of finite control set model predictive control in power electronics," *IEEE Trans. Ind. Informat.*, vol. 9, no. 2, pp. 1003–1016, May 2013.

[15] J. Rodriguez and P. Cortes, *Predictive Control of Power Converters and Electrical Drives*. Hoboken, NJ, USA: Wiley, 2012.

[16] E. Fuentes, J. Rodriguez, C. Silva, S. Diaz, and D. Quevedo, "Speed control of a permanent magnet synchronous motor using predictive current control," in *Proc. 6th IEEE Int. Power Electron. Motion Control Conf. (IPEMC'09)*, May 2009, pp. 390–395.

[17] M. Preindl and S. Bolognani, "Model predictive direct torque control with finite control set for PMSM drive systems, part 1: Maximum torque per ampere operation," *IEEE Trans. Ind. Informat.*, vol. 9, no. 4, pp. 1912–1921, Nov. 2013.

[18] M. Preindl and S. Bolognani, "Model predictive direct torque control with finite control set for PMSM drive systems, part 2: Field weakening operation," *IEEE Trans. Ind. Informat.*, vol. 9, no. 2, pp. 648–657, May 2013.

[19] Y. Cho, K.-B. Lee, J.-H. Song, and Y. Lee, "Torque-ripple minimization and fast dynamic scheme for torque predictive control of permanent-magnet synchronous motors," *IEEE Trans. Power Electron.*, vol. 30, no. 4, pp. 2182–2190, Apr. 2015.

[20] M. Preindl and S. Bolognani, "Model predictive direct speed control with finite control set of PMSM drive systems," *IEEE Trans. Power Electron.*, vol. 28, no. 2, pp. 1007–1015, Feb. 2013.

[21] E. Fuentes, D. Kalise, J. Rodriguez, and R. Kennel, "Cascade-free predictive speed control for electrical drives," *IEEE Trans. Ind. Electron.*, vol. 61, no. 5, pp. 2176–2184, May 2014.

[22] L. Dosiek and P. Pillay, "Cogging torque reduction in permanent magnet machines," *IEEE Trans. Ind. Electron.*, vol. 43, no. 6, pp. 1565–1571, Nov. 2007.

[23] G. A. Baker and J. L. Gammel, *Pade Approximant in Theoretical Physics*. Amsterdam, The Netherlands: Elsevier, 1970.

[24] R. Lorenz and K. Van Patten, "High-resolution velocity estimation for all-digital, ac servo drives," *IEEE Trans. Ind. Electron.*, vol. 27, no. 4, pp. 701–705, Jul. 1991.

[25] P. Cortes *et al.*, "Guidelines for weighting factors design in model predictive control of power converters and drives," in *Proc. IEEE Int. Conf. Ind. Technol.*, Feb. 2009, pp. 1–7.

[26] R. Aguilera, P. Lezana, and D. Quevedo, "Finite-control-set model predictive control with improved steady-state performance," *IEEE Trans. Ind. Informat.*, vol. 9, no. 2, pp. 658–667, May 2013.

Andrés Mora (S'13) was born in Santiago, Chile, in 1984. He received the Eng. and M.Sc. degrees in electrical engineering from the Universidad Técnica Federico Santa María (UTFSM), Valparaíso, Chile, in 2010. He is currently working toward the Ph.D degree in electrical engineering at the Universidad de Chile, Santiago, Chile.

Since 2011, he has been an Assistant Professor with UTFSM. His research interests include power converters, digital control of electrical drives, and electrical machine theory.

Álvaro Orellana was born in La Serena, Chile, in 1988. He received the Eng. degree in electrical engineering from the Universidad Técnica Federico Santa Maria (UTFSM), Valparaíso, Chile, in 2013.

He has been an Electrical Engineer in the power converter industry with GE Power Conversion, Santiago, Chile, and also a Lecturer with the Department of Electrical Engineering, UTFSM, since 2013. His research interests include power converters, electrical drives, and electrical machines.

Jorge Juliet (M'05) received the Eng. degree in electrical engineering from the Universidad Técnica Federico Santa María (UTFSM), Valparaíso, Chile, in 1997, and the Dr.-Ing. degree in electrical engineering from the Electrical Machines and Drives Group, Bergische Universität Wuppertal, Wuppertal, Germany, in 2005.

Since 1997, he has been with the Departamento de Ingeniería Eléctrica, UTFSM. His research interests include electrical machines theory, digital control of electrical drives, and power electronics.

Roberto Cárdenas (S'95–M'97–SM'07) was born in Punta Arenas, Chile. He received the B.Sc. degree in electrical engineering from the University of Magallanes, Punta Arenas, Chile, in 1988, and the M.Sc. degree in modern electronics and Ph.D degree in electrical and electronic engineering from the University of Nottingham, Nottingham, U.K., in 1992 and 1996, respectively.

From 1989 to 1991 and from 1996 to 2008, he was a Lecturer with the University of Magallanes. From 1991 to 1996, he was with the Power Electronics Machines and Control Group (PEMC Group), University of Nottingham. From 2009 to 2011, he was with the Department of Electrical Engineering, University of Santiago, Santiago, Chile. He is currently a Professor of Power Electronics and Drives with the Department of Electrical Engineering, University of Chile, Santiago, Chile. His research interests include control of electrical machines, variable-speed drives, and renewable energy systems.

Prof. Cárdenas was the recipient of the Best Paper Award from the IEEE TRANSACTIONS ON INDUSTRIAL ELECTRONICS in 2005.